RSC Advances

ROYAL SOCIETY OF CHEMISTRY

www.rsc.org/advances

Type-II α-In_2S_3/In_2O_3 nanowire heterostructures: evidence of enhanced photo-induced charge separation efficiency

Li-Chia Tien* and Jhih-Lin Shih

Department of Materials Science and Engineering, National Dong Hwa University, Shoufeng, Hualien 974, Taiwan

Abstract

Separation of photo-induced charges is crucial in controlling the performance of photocatalysts, photochemical cell, and photovoltaic devices. We developed a controlled synthesis of α-In_2S_3/In_2O_3 nanowire heterostructures by a hydrothermally assisted sulfurization process. Structural characterization reveals that two distinct nanowire heterostructures: α-In_2S_3 nanoparticles decorated In_2O_3 nanowires and α-In_2S_3/In_2O_3 core-shell nanowires were obtained by controlling the pH condition during sulfurization process. Optical characterization results show α-In_2S_3/In_2O_3 nanowire heterostructures exhibit a significantly decreased visible light emission and enhanced visible light absorption compare with the pure In_2O_3 nanowires, revealing an efficient photo-induced charge separation efficiency exists. The band offsets of α-In_2S_3/In_2O_3 nanowire heterostructures were determined by X-ray photoemission spectroscopy and a type-II band alignment at interface is confirmed. Time-resolved photoluminescence results reveal that the α-In_2S_3 nanoparticles/In_2O_3 nanowires exhibit significant photo-induced carrier life time improvement compare with α-In_2S_3/In_2O_3 core-shell nanowire, due to a shorter charge carrier transport path, which ensures rapid charge separation at interface. Because of the staggered band offset which promoted effective charge separation, the α-In_2S_3/In_2O_3 nanowire heterostructures exhibited enhanced photocatalytic activities under visible light illumination, demonstrating their promising potentials in relevant photo-conversion applications.

Keywords: heterostructure; nanowires; charge separation; oxides; sulfides

* To whom correspondence should be addressed: lctien@mail.ndhu.edu.tw

TEL:+886-3-863-4208, FAX: +886-3-863-4200

1. Introduction

Owing to the high degree of complexity, semiconductor heterostructures exhibit superior properties which are difficult to achieve from single material. Efforts have been made in developing various semiconductor heterostructures.[1-3] The formation of semiconductor heterostructures is an effective way to increase the photo-induced charge separation efficiency and the photocatalytic performance. According to the alignment of the bands, type-II semiconductor heterostructures composed of two components with a staggered band offset. The position of valence and conduction bands of one semiconductor is higher than that of the other semiconductor. The difference in band alignment cause the spatial separation of the electron and hole pairs, may result in longer carrier lifetime that has desirable characteristics for potential applications such as highly efficient photocatalysts, photochemical cell, and photovoltaic devices.[4]

A wide band gap semiconductor material coupled with a narrow band gap semiconductor material can effectively improve its solar energy utilization efficiency since the adsorption spectrum can be extended to the whole solar spectrum.[5, 6] For this purpose, the outer shell semiconductor should be a strong visible light absorption material, and the band alignment between the outer shell and the inner core semiconductor should be with a staggered band offset in the ideal type-II semiconductor heterostructures. Consequently, the photo-induced electrons and holes would transfer toward opposite side of the heterojunctions, carrier lifetime can be substantially increased. Recently, one-dimensional (1D) semiconductor nanostructures with type-II heterostructures have drawn much attention due to their enhanced photocatalytic activity and visible light absorption ability. Various nanostructures with type-II band alignment have been synthesized and demonstrated, such as core-shell nanoparticles, nanoparticles decorated nanowires, core-shell nanowires, etc.[7-11] The 1D core-shell nanowires provide a direct electrical pathway for the rapid transport of photo-induced

carriers, which ensures rapid charge separation at interface. Furthermore, the formation of nanowire heterostructures can be formed by decorating the nanowire surface with nanoparticles, which has been confirmed as an efficient approach to increase visible light absorption and enhance the photo-induced carrier separation efficiency. For photocatalytic applications, the nanoparticle size and its surface properties are two important factors influencing the photocatalytic activity and the separation efficiency of photo-induced electron-hole pairs because the photocatalytic reactions take place at or near the surface.[12] For photovoltaic devices, nanowire heterostructures are predicted to facilitate large improvements in efficiency over planar geometries by combining optimal absorption of photons with efficient collection of generated carriers.[13, 14]

Indium oxide (In_2O_3) nanowires have been widely used in chemical sensors and field emitters.[15-18] Combining In_2O_3 nanowires with narrow band gap semiconductor can efficiently improve their visible light response and increase charge separation efficiency by reducing the probability of electron-hole recombination. Indium sulfide (In_2S_3) is an important III-VI semiconductor with band gap of 2.0–2.3 eV that has been extensively studied due to its applicability in solar cells, visible-light-active photocatalysts, and optoelectronic device applications.[19] Owing to their diverse applications, efforts have been devoted to the synthesis of nanostructured In_2S_3 such as nanotubes, nanocrystals, nanoflakes, and nanoplates.[20-23] In particular, further combining In_2O_3 and In_2S_3 by forming heterostructured nanostructures would be of great interests in regard to achieving desired properties. For example, Li *et al.* have shown In_2O_3/In_2S_3 core-shell nanocubes with enhanced photo-electrochemical performance.[24] The In_2O_3/In_2S_3 core-shell nanorods have been demonstrated for photocatalytic hydrogen generation.[25] In these cases, the In_2O_3/In_2S_3 nanowire heterostructures have shown better charge collection, enhanced light absorption, and slow photo-induced charge carrier recombination rate. However, their band alignment

is still controversial, diverse band alignment such as type-I and type-II band alignment has been reported.[24-26] The inconsistency for the band alignment is mainly be attributed to the lack of well-defined In_2S_3/In_2O_3 interfaces that are amenable to experimental techniques. Therefore, a fundamental study that can verify the band alignment and correlation between band alignment and photo-induced charge separation efficiency of In_2S_3/In_2O_3 nanowire heterostructures is of great importance to be studied.

In this work, two distinct type-II semiconductor nanowire heterostructures: α-In_2S_3 nanoparticles decorated In_2O_3 nanowires (α-In_2S_3 NP/In_2O_3 NW) and α-In_2S_3 /In_2O_3 core-shell nanowires (α-In_2S_3/In_2O_3 C-S NW) were synthesized by a simple hydrothermally assisted sulfurization process. Their structural, optical, and photocatalytic properties were carefully examined by a variety of characterization tools. The band offsets of α-In_2S_3/In_2O_3 nanowire heterostructures were identified as a type-II band alignment and the direct evidence of enhanced photo-induced charge separation efficiency were observed by photoluminescence, time-resolved photoluminescence, and visible-light photocatalytic activity measurements. Consequently, both α-In_2S_3/In_2O_3 nanowire heterostructures show enhanced visible light absorption and visible light driven photocatalytic activity due to efficient charge separation and high charge transfer efficiency of photo-induced electrons. Of particular interest is the time-resolved photoluminescence results show that the α-In_2S_3 NP/In_2O_3 NW exhibit significant carrier life time improvement compared to α-In_2S_3/In_2O_3 C-S NW, due to a shorter charge carrier transport path, which ensures rapid charge separation at interface. Practically, the study will be of fundamental importance to understand the effect of surface geometry on the photo-induced carrier separation efficiency of type-II nanowire heterostructures.

2. Experimental

2.1 Synthesis of α-In_2S_3/In_2O_3 nanowire heterostructures

Synthesis of In_2O_3 nanowires. α-In_2S_3/In_2O_3 nanowire heterostructures were synthesized using a thermal evaporation method followed by a hydrothermally assisted sulfurization process. First, the growth of In_2O_3 nanowires was carried out using a thermal evaporation process. In brief, a horizontal tube furnace (Lindberg Blue) with three independent heating zones was used for the sample growth. Indium powder (1.2 g, 99.99%, Alfa Aesar) was used as source material, put in an alumina boat and placed at center of the quartz tube. Thin layers (5 nm) of Au were deposited on the silicon (001) substrates by DC sputtering. The substrates were put in another boat and placed at downstream. The furnace was then heated to 750°C at a rate of 10°C/min. Once furnace reaches growth temperature, the oxygen and argon mixtures (5/95 SCCM) were fed into quartz tube. The growth temperature was estimated to be 450°C in a background pressure of 0.5 Torr during growth. The typical growth time was 1 h.

Hydrothermally assisted sulfurization process. The as-grown In_2O_3 nanowires on silicon (001) substrate was placed in a Teflon-lined stainless steel autoclave (23 mL). In a typical process, 0.1 g of thioacetamide (TAA, 99%, Alfa Aesar) was suspended in 10 mL of deionized water. The pH values of the suspension was adjusted to pH=6, 4 and 2 by adding small amount of HCl (0.1M) solution. After adding the TAA solution, the autoclave was then sealed and maintained at 150°C for 4 h then cooled to room temperature naturally. The samples were washed with ethanol and deionized water for three cycles to remove ionic remnants, then dried at 60°C for 1h.

2.2 Sample characterization

All samples were characterized using a field emission scanning electron microscopy (FE-SEM, JEOL, JSM-7000F), energy-dispersive X-ray spectroscopy (EDX), X-ray diffractometer (XRD, Rigaku, D/Max 2500V), X-ray photoelectric spectroscopy (XPS, Thermo Scientific, K-Alpha), and high-resolution transmission electron microscopy (HR-TEM, Philips, FEI Tecnai G2). XPS measurements were

made using an Al K_α ($h\nu$ = 1486.6 eV) source that was equipped with a micro-focused monochromator (spot size: 30–400 μm). The spectra are presented in terms of binding energy with reference to the binding energy of carbon 1s (284.85 eV). For HR-TEM observation, the samples were ultrasonically dispersed in methanol, and then several drops of the suspension were placed on amorphous carbon films, which were supported by copper grids and dried in air. Steady-state photoluminescence (PL) measurements of samples were made using a spectrometer (Horiba J-Y, iHR 550) as the optical dispersion unit and a CCD (Horiba J-Y, Synapse) was used for optical detection. An He-Cd (λ=325 nm) laser was used as the excitation source. Time-resolved PL spectra of samples were recorded at 495 nm with 303 nm excitation at room temperature using a multifunction steady state and transient state fluorescence spectrometer (Edinburgh Instruments, FLSP920). All measurements were performed at room temperature.

2.3 Photocatalytic activity test

The photocatalytic activity of samples were evaluated by the degradation of organic dye in aqueous solution under visible-light irradiation using a 500W Xe lamp with a cutoff filter (λ>420 nm). The photocatalytic activity was evaluated by the decomposition of methyl blue (MB) in a deionized water solution with an initial concentration of 1×10^{-5} M. A sample size of 1 cm^2 was added to 10 mL of dye solution in a beaker covered with a quartz plate. Before irradiation, the samples were put in the dark for 30 min to ensure stable adsorption. After desired time intervals, the concentration of solution was analyzed by recording the characteristic absorption of MB (664 nm) using an Ultraviolet-visible spectrometer (UV/Vis, Hitachi, U-3900). The estimated weight of α-In_2S_3/In_2O_3 nanowire heterostructures was in the range of 0.13 to 0.18 mg for the samples considered.

3 Results and discussion

3.1 Structural characterization of α-In_2S_3/In_2O_3 nanowire heterostructures

The surface morphologies of samples were characterized using FE-SEM. Figure 1(a) shows top-view FE-SEM image of as-grown In_2O_3 nanowires on silicon substrate. The as-synthesized product consist of a large quantity of 1D nanostructures with relatively uniform diameter and high aspect ratio. The In_2O_3 nanowires are approximately 90–110 nm in diameter and approximately 1–3 μm long. These In_2O_3 nanowires were used as templates for the synthesis of α-In_2S_3/In_2O_3 nanowire heterostructures by a hydrothermally assisted sulfurization process. Figure 1(b) displays FE-SEM image of In_2O_3 nanowires after sulfurization at pH value of 6. The size of the obtained nanowires decreases slightly and a mixture of nanowires and nanowhiskers are observed. Decreasing the pH value to 4, the size of the nanowires decreases further in diameter as shown in Fig. 1(c). For further decrease in pH value to 2, large quantity of hierarchical nanostructures were formed. (Fig. 1(d)) The inset shows optical image of sample prepared at different pH values. It can be seen that there was a striking color change from yellow to orange as the pH value changed from 6 to 2. From the above observations, the morphological characteristics of the α-In_2S_3/In_2O_3 nanowire heterostructures are controlled by the pH condition of solution during hydrothermally assisted sulfurization process.

The structural properties of the samples herein were characterized with XRD. Figure 2 shows the X-ray diffraction patterns of as-grown In_2O_3 nanowires and In_2O_3 nanowires after sulfurization at different pH values. All patterns of as-grown sample were indexed to the In_2O_3 cubic bixbyite structure with a lattice constant of a =b=c=10.12Å (JCPDS PDF 71-2194). Following sulfurization at pH value of 6, the peaks at 2θ values of 23.4, 27.5, 28.8, 33.3, 43.7, and 47.8 can be indexed to (220), (311), (222), (400), (511), and (440) crystal planes of cubic α-In_2S_3 (JCPDS PDF 65-0459), respectively. Two sets of XRD diffraction peaks of cubic In_2O_3 and cubic α-In_2S_3 can be clearly observed. The diffraction peak intensity ratio corresponding to In_2O_3 and

α-In_2S_3 decrease gradually with decreasing pH value. No impurity peaks were observed, confirming the high purity of the products. Furthermore, the intensity of In_2O_3 diffraction peaks decreases significantly as the pH value decreases from 6 to 4, suggesting the reaction rate for the sulfurization of In_2O_3 nanowires has been increased under low pH conditions. In addition, it is worth noting that the In_2O_3 diffraction peaks were eliminated when pH value changed to 2, which indicates that the formation of pure α-In_2S_3 phase was completed by hydrothermally assisted sulfurization process. Based on the above observation, the formation process of α-In_2S_3 on In_2O_3 nanowires can be achieved by using TAA as a reducing agent and sulfur source, which contribute to the formation of α-In_2S_3/In_2O_3 nanowire heterostructures.

TEM was utilized to provide further structural characterization of samples. Figure 3(a) shows a low-magnification image of hierarchial nanostructures obtained at pH value of 2, revealing the nanostructures to be a collection of many assembled α-In_2S_3 nanoflakes. Figure 3(b) shows TEM image of a single α-In_2S_3 nanoflake, the lateral dimension of single nanoflake was estimated to be about 200–250 nm. The selected-area electron diffraction (SAED) was used to confirm the crystal structure of α-In_2S_3 nanoflakes. Figure 3(c)–(d) shows the SAED pattern of a single α-In_2S_3 nanoflake taken at different zone axis, the sharp diffraction patterns indicate that these nanoflakes are single crystal cubic α-In_2S_3 structure. Therefore, the phase purity of α-In_2S_3 is confirmed.

The growth of α-In_2S_3/In_2O_3 nanowire heterostructures is based on the relatively complex sequence of equilibrium processes which occur in the solution, as described below. A series of consecutive reactions, which lead to generation of sulfide ions in the reaction begins with the hydrolysis of thioacetamide under acidic pH conditions:[27]

$$CH_3CSNH_{2(aq)} + H_2O_{(l)} \rightleftharpoons CH_3CONH_{2(aq)} + H_2S_{(aq)} \quad (1)$$

Hydrogen sulfide dissociates in the following steps:

$$H_2S_{(aq)} + H_2O_{(aq)} \rightleftharpoons HS^-_{(aq)} + H_3O^+_{(aq)} \quad (2)$$

$$HS^-_{(aq)} + H_2O_{(l)} \rightleftharpoons S^{2-}_{(aq)} + H_3O^+_{(aq)} \quad (3)$$

The described consecutive reaction enabled us to control the concentration of sulfide anions in the reaction, and consequently to provide conditions for controlled nucleation. The crystal growth of α-In_2S_3 on In_2O_3 nanowires surface by following reaction:

$$2In^{3+}_{(aq)} + 3S^{2-}_{(aq)} \rightleftharpoons In_2S_{3(s)} \quad (4)$$

To control the growth rate of In_2S_3, another main concern is the metal ion concentration in the solution. Since In_2O_3 can be dissolved in acidic solutions, therefore, the concentration of In^{3+} ions in the reaction can be controlled by adjusting the pH value of solution. According to the XRD results, it was concluded that the growth rate of In_2S_3 process are predominately controlled by adjusting pH values of solution.

Controlling the shell thickness and morphology is an important issue in the preparation of core/shell heterostructure nanostructures because it may crucially affects the electrical and optical properties of the heterostructures.[4, 28] Comprehensive investigations on the morphological and compositional properties of the α-In_2S_3/In_2O_3 nanowire heterostructures was further confirmed by TEM and STEM. Figure 4(a) shows a TEM image of α-In_2S_3/In_2O_3 nanowire heterostructure obtained at pH of 6. The nanowire exhibited a diameter approximately 150 nm. The TEM image shows that occasional α-In_2S_3 nanoparticles have been deposited on the nanowire surface along the axial direction. The mean diameter of α-In_2S_3 nanoparticles is typically 5–50 nm in diameter and the distribution of α-In_2S_3 nanoparticles on the In_2O_3 nanowire surface is microscopically discontinuous. Spatial elemental distributions of In, O, and S were confirmed by STEM elemental mapping and EDX line profiling of the nanowire. EDX line scanning across the nanowire heterostructure reveals that the profiles of In and O have a broad spectrum throughout the entire diameter whereas the peaks for S are only prominent at specific region (Fig. 4(b)), where α-In_2S_3 nanoparticles were located. The

elemental maps, in Fig. 4(c), clarify the distribution for each constituting element (In, O, and S) in the α-In_2S_3/In_2O_3 nanowire heterostructure. It is concluded that the obtained sample are α-In_2S_3 nanoparticles decorated In_2O_3 nanowires (α-In_2S_3 NP/In_2O_3 NW). Figure 4(d) shows a TEM image of α-In_2S_3/In_2O_3 nanowire heterostructure obtained at pH of 4. The nanowire exhibited a slightly smaller diameter around 120 nm, probably because of the high etching rate of In_2O_3 nanowire surface under low pH conditions. Unlike the nanowires obtained at pH value of 6, the nanowire present relatively smooth surfaces indicating the layer growth dominates. The presence of the α-In_2S_3 layer is confirmed by both chemical and structural analyses above. Both EDX line-scan (Fig. 4(e)) and elemental mapping (Fig. 4(f)) results confirm a highly uniform α-In_2S_3 coating over In_2O_3 nanowires was obtained at pH of 4. The nanowire exhibit a core-shell nanowire heterostructure and the shell thickness is estimated to be approximately 20–30 nm by mass-contrast of HR-TEM image. It is worth nothing that while the bulk α-In_2S_3/In_2O_3 heterostructures are difficult to grow due to the large lattice mismatch (~6.4%), however, the feasibility to grown heterostructures nanowires with large lattice mismatch has been demonstrated.[28-32] In general, the growth of heterostructured materials is limited by lattice mismatches in planar system, which may result in poor-quality interfaces with high density of defects. The nanowire geometry provides strain modifications or reductions to the growth of materials that may be unstable when grown on thin film or bulk substrates. Therefore, the nanowire heterostructures provide an ideal platform to relieve strain at interfaces, reducing the generation of defects.[32] We attribute the formation of α-In_2S_3/In_2O_3 core-shell nanowire heterostructure herein to the ability of the strain relaxation of nanowire geometry.

3.2 Optical properties of α-In_2S_3/In_2O_3 nanowire heterostructures

The optical properties of α-In_2S_3/In_2O_3 nanowire heterostructures were examined using PL and UV/vis absorption spectroscopy at 300K. Figure 5(a) displays the PL

spectra of pure In_2O_3 nanowires, α-In_2S_3/In_2O_3 nanowire heterostructures, and pure α-In_2S_3 nanoflakes at 300K. The pure In_2O_3 nanowires exhibits an intense visible emission ranging from 450 nm to 900 nm, originates from the recombination of donor from oxygen vacancy band (V_O) to the acceptor band consists of indium vacancy (V_{In}) or oxygen-indium vacancy pairs (V_O-V_{In}).[34] The pure α-In_2S_3 nanoflakes reveal a strong red emission centered at 890 nm, attribute to defect emission possibly originates from transitions between different defect levels such as sulfur vacancy (V_S) and indium vacancy (V_{In}).[35] As to α-In_2S_3/In_2O_3 nanowire heterostructure, a significant depression in PL emission was observed. It has been reported that the type-II band alignment in heterostructures would facilitate the separation of photo-induced charge carriers, resulting in quenching of PL intensity.[36, 37] We attribute the photo-induced charge transfer from α-In_2S_3 to In_2O_3 is responsible for the emission quenching of α-In_2S_3/In_2O_3 nanowire heterostructures.

Figure 5(b) depicts the UV/vis absorption spectra of pure In_2O_3 nanowires, α-In_2S_3/In_2O_3 nanowire heterostructures, and pure α-In_2S_3 nanoflakes. The pure In_2O_3 nanowires have no absorbance in the visible light, with an absorption edge of about 420 nm, which is consistent with the optical band gap of In_2O_3. However, the α-In_2S_3/In_2O_3 nanowire heterostructures show a red shift of the absorption edge to ~600 nm. The α-In_2S_3 nanoflakes exhibit a strong absorbance in the visible light with an absorption edge around 600 nm, which is corresponding well with the band gap of α-In_2S_3 in the literature.[38] The results herein are in accordance with the color changing from yellow to orange shown in Fig. 1, confirming the visible light absorption can be increased by deposition of α-In_2S_3 on In_2O_3 nanowires.

3.3 Band offsets of α-In_2S_3/In_2O_3 nanowire heterostructures

For semiconductor heterostructures, knowledge of the valence and conduction band offsets is of particular importance. The band offsets of α-In_2S_3/In_2O_3 nanowire

heterostructures were determined by XPS. The XPS survey spectra in Fig. 6(a) reveal only In, O, S, and C, indicating the high purity of the samples. Figures 6(b)–(d) present high-resolution XPS spectra of In 3*d*, O 1*s*, and S 2*p*, respectively. For pure In_2O_3 nanowires, the emission from In 3*d* core levels, exhibiting two intense peaks at 451.5 and 443.95 eV for In $3d_{3/2}$ and $3d_{5/2}$, respectively, is highly consistent with the highest oxidation state of indium (In^{3+}). The peaks shifted slightly toward high binding energy when α-In_2S_3 was formed on In_2O_3 nanowires. This may due to the change in the chemical environment of the indium atoms involving a redistribution of the valence electron changes, which influenced the potential of the core electrons that results in the shift of the binding energies. The O 1*s* and S 2*p* core-level spectra were fitted using Shirley and Voigt functions. The oxygen atoms that are bound to indium atoms in the structure give rise to an O 1*s* peak close to 529.5 eV, and a higher binding energy component, centered at 531.5 eV is attributed to adsorbed hydroxyls (Fig. 6(c)). The S 2*p* core-level spectra shown in Fig. 6(d) were deconvoluted into two components, located at 161.4 and 161.68 eV, respectively. The lower binding energy peak is attributed to In-S of α-In_2S_3, whereas the higher energy peak is assigned to the S-O due to surface oxidation. Moreover, an additional low intensity, high binding energy component centered at 163.1 eV was also required. The extra component is attributed to trace amount of S_8 on the surface. The binding energies for In 3*d* and S 2*p* of α-In_2S_3 nanoflakes were in accordance with the data reported for In_2S_3 in the literature.[39]

The valence band XPS spectra are shown in Fig. 6(e). The position of the valence band maximum (VBM) with respect to the Fermi level was determined by the intersection of linear fits to the leading edge of the valence band photoemission and the background. The valence band offsets of α-In_2S_3/In_2O_3 nanowire heterostructures were determined from the energy separation between the core-levels in the α-In_2S_3/In_2O_3 sample and the VBM to core level separation in pure In_2O_3 and α-In_2S_3 nanoflakes, as

follows:[40, 41]

$$E_{VBO} = E_{O\ 1s}^{In_2S_3/In_2O_3} - E_{S\ 2p_{3/2}}^{In_2S_3/In_2O_3} - \left(E_{O\ 1s}^{In_2O_3} - E_{VBM}^{In_2O_3}\right) + (E_{S\ 2p_{3/2}}^{In_2S_3} - E_{VBM}^{In_2S_3})$$

Using the optical band gap energy of 2.93 and 2.03 eV, determined from absorption spectra (Fig. 5(b)) of pure In_2O_3 nanowires and α-In_2S_3 nanoflakes, both α-In_2S_3/In_2O_3 nanowire heterostructures are found to have a type-II band alignment as shown in Fig. 7, with a corresponding valence band offset of 1.67 and 1.72 eV, respectively.

Although the carrier concentration of α-In_2S_3 is crucial to explain the differences in band offset, the nanoscale geometry makes them inherently difficult to characterize. Here, we attribute the variation of band offset to different carrier concentration of α-In_2S_3 due to different surface geometry of nanowire heterostructures. It is well known that the surface to volume ratio of nanoparticles is larger than nanowires, and the carrier concentration of α-In_2S_3 is altered by the adsorption and depletion of surface adsorbed molecules. Due to the difference in geometry and surface area, the surface depletion region of α-In_2S_3 NP/In_2O_3 NWs is slightly larger than those of α-In_2S_3/In_2O_3 C-S NW. Therefore, a lower carrier concentration of α-In_2S_3 nanoparticles on In_2O_3 nanowire was found, which leads to a smaller valence band offset in α-In_2S_3 NP/In_2O_3 NW.

3.4 Measurement of photo-induced charge separation efficiency

The above results indicate both α-In_2S_3/In_2O_3 nanowire heterostructures are of type-II band alignment. We expect that the photo-induced charge separation efficiency could be enhanced significantly in α-In_2S_3/In_2O_3 nanowire heterostructures. Time-resolved PL has been widely employed to investigate the kinetics of photo-induced process occurring in materials.[42-44] The interfacial charge transfer property of type-II α-In_2S_3/In_2O_3 nanowire heterostructure has been investigated by time-resolved PL. Figure 8 represents the time-resolved PL spectra of pure In_2O_3 and α-In_2S_3/In_2O_3 nanowire heterostructures. Exponential decay time constants were obtained using non-linear

fitting to a model function that composed by the convolution of a Gaussian-fitted instrument response function (IRF) and an exponential decay function. In the case of pure In_2O_3 nanowires, the fitted decay constant is 0.12 ns, which is far shorter than the full width half maximum (FWHM) of IRF (1.45 ns), indicating the photo-induced carrier recombination lifetime is shorter than the resolution of instrument. However, the decay constants of α-In_2S_3/In_2O_3 C-S NWs (pH=4) and α-In_2S_3 NP/In_2O_3 NWs (pH=6) are 0.3 and 0.6 ns, respectively, that is one fourth of the FWHM of IRF. This slow recombination process can be understood based on the spatially separated electrons and holes in a type-II band alignment. Notably, there is a clear time delay (~0.35 ns) in the luminescence peak for α-In_2S_3 NP/In_2O_3 NWs, indicating the recombination rate has been decreased. The α-In_2S_3 NP/In_2O_3 NWs exhibit significant photo-induced carrier life time improvement compared to α-In_2S_3/In_2O_3 C-S NWs, possibility due to a shorter charge carrier transport path, which ensures rapid charge separation at interface. Further study is needed to elucidate the effect of morphology and geometry of out shell material on interface charge transfer efficiency.

3.5 Visible-light driven photocatalytic activity

To verify the photo-induced charge separation efficiency of α-In_2S_3/In_2O_3 nanowire heterostructures, we performed photo-degradation experiments by using Methyl Blue (MB) as the probe molecule. The decolorization of MB under visible light illumination can be used to evaluate the photo-induced charge separation efficiency and visible light responses of the sample. Figure 9(a) shows the photo-degradation of MB as a function of irradiation time over different samples. For the adsorption in the dark, all samples exhibited comparable adsorption capacity, which is probably attribute the small amount of catalysts (0.13–0.18 mg). It is clearly seen that the pure In_2O_3 nanowires do not show any photocatalytic activity under visible light illumination due to its relatively wide band gap energy (2.93 eV). The α-In_2S_3 nanoflakes show visible-light driven

photocatalytic activity on account of their small optical band gap (2.03 eV) and large surface area. The results is not surprising because In_2S_3 nanostructures have been reported with visible-light photocatalytic activity.[45-48] Both α-In_2S_3/In_2O_3 nanowire heterostructures exhibit enhanced photocatalytic activity under visible light illumination, which can be accounted for the effective charge separation efficiency and enhanced visible light absorption of type-II heterostructure. Under light irradiation, the photo-induced electrons from the conduction band of α-In_2S_3 transfer into In_2O_3, and holes in the valence band of In_2O_3 transfer to α-In_2S_3. The photo-induced holes were trapped by surface hydroxyl or water molecules to form high reactive hydroxyl radical species (·OH), which will oxidize dye to CO_2. Meanwhile, the electrons were captured by O_2 on the surface, which results in the formation of reactive peroxide O_2^-. The transfer of electrons and holes in α-In_2S_3/In_2O_3 nanowire heterostructures increases the yield and lifetime of charge carriers, as well as reduces the recombination of electrons and holes. The α-In_2S_3/In_2O_3 nanowire heterostructures not only extend the visible light absorption but also slow down the electron-hole pair recombination rate. Both these two effects contributed to enhanced visible light photocatalytic activity. Furthermore, the α-In_2S_3 nanoparticles could provide a shorter pathway for the migration of photo-induced charge carriers, whereas the heterojunction at α-In_2S_3/In_2O_3 interface could reduce the recombination probability of photo-induced electrons and holes through an internal electric field and thus leads to a higher photocatalytic efficiency. Specifically, the α-In_2S_3 nanoparticles decorated In_2O_3 nanowire heterostructure shows a higher photocatalytic activity compared to α-In_2S_3/In_2O_3 core-shell nanowire, attributed to the significant carrier life time improvement observed in TR-PL results.

For sustainability concern, the α-In_2S_3 nanoparticles decorated In_2O_3 nanowire heterostructure sample was examined for their anti-photocorrosion properties. The photocatalytic stability test under visible light irradiation of α-In_2S_3 nanoparticles

decorated In_2O_3 nanowire heterostructure sample is shown in Fig. 9(b). The sample exhibited good photo-stability and showed no noticeable loss of photocatalytic activity after 4 cycles. The results suggest that α-In_2S_3/In_2O_3 nanowire heterostructures exhibit a stable activity toward degradation of organic pollutant.

4 Conclusions

This work demonstrated a hydrothermally assisted sulfurization process for synthesizing α-In_2S_3/In_2O_3 nanowire heterostructures. Two distinct nanowire heterostructures: α-In_2S_3 nanoparticles decorated In_2O_3 nanowires and α-In_2S_3/In_2O_3 core-shell nanowires were obtained respectively, by controlling the pH condition during sulfurization process. The α-In_2S_3/In_2O_3 nanowire heterostructures exhibit a significantly decreased visible light emission and enhanced visible light absorption compared with the pure In_2O_3 NWs, revealing an efficient photo-induced charge separation efficiency. The band offset of α-In_2S_3 /In_2O_3 nanowire heterostructures was identified as a type-II band alignment. Time-resolved photoluminescence results indicates that the type-II α-In_2S_3/In_2O_3 nanowire heterostructures exhibit significant photo-induced carrier life time improvement, which is caused by promoted effective charge separation of staggered band offset. By measuring the visible-light driven photocatalytic activity of samples, we demonstrated that the α-In_2S_3 nanoparticles decorated In_2O_3 nanowire heterostructure shows a high photocatalytic activity, which can be well accounted for by the carrier life time improvement of sample. With the significant photo-induced charge separation property and visible absorption capability, the present α-In_2S_3/In_2O_3 nanowire heterostructures may be promising in relevant photo-conversion applications.

Acknowledgments

The authors would like to thank the Ministry of Science and Technology of the Republic of China, Taiwan, for financially supporting this research under Contract No.

MOST 104-2112-M-259-002.

References

1. F. A. Ponce and D. P. Bour, *Nature*, 1997, **386**, 351-359.
2. Y. Ohno, D. K. Young, B. Beschoten, F. Matsukura, H. Ohno and D. D. Awschalom, *Nature*, 1999, **402**, 790-792.
3. J. K. Hyun, S. Zhang and L. J. Lauhon, in *Annual Review of Materials Research, Vol 43*, ed. D. R. Clarke, 2013, vol. 43, pp. 451-479.
4. Y. Wang, Q. Wang, X. Zhan, F. Wang, M. Safdar and J. He, *Nanoscale*, 2013, **5**, 8326-8339.
5. A. Kudo and Y. Miseki, *Chemical Society Reviews*, 2009, **38**, 253-278.
6. Z. Zhang, W. Wang, L. Wang and S. Sun, *Acs Applied Materials & Interfaces*, 2012, **4**, 593-597.
7. Y. Tak, H. Kim, D. Lee and K. Yong, *Chemical Communications*, 2008, DOI: 10.1039/b810388g, 4585-4587.
8. P. Wu, T. Sun, Y. Dai, Y. Sun, Y. Ye and L. Dai, *Crystal Growth & Design*, 2011, **11**, 1417-1421.
9. D. Sarkar, C. K. Ghosh, S. Mukherjee and K. K. Chattopadhyay, *Acs Applied Materials & Interfaces*, 2013, **5**, 331-337.
10. M. Basu, N. Garg and A. K. Ganguli, *Journal of Materials Chemistry A*, 2014, **2**, 7517-7525.
11. C. Cheng, A. Amini, C. Zhu, Z. Xu, H. Song and N. Wang, *Scientific Reports*, 2014, **4**, 4181.
12. C. J. Lin, Y. H. Yu and Y. H. Liou, *Applied Catalysis B-Environmental*, 2009, **93**, 119-125.
13. Y. B. Tang, Z. H. Chen, H. S. Song, C. S. Lee, H. T. Cong, H. M. Cheng, W. J. Zhang, I. Bello and S. T. Lee, *Nano Letters*, 2008, **8**, 4191-4195.
14. K. Wang, J. J. Chen, Z. M. Zeng, J. Tarr, W. L. Zhou, Y. Zhang, Y. F. Yan, C. S. Jiang, J. Pern and A. Mascarenhas, *Applied Physics Letters*, 2010, **96**, 123105.
15. C. Li, D. H. Zhang, X. L. Liu, S. Han, T. Tang, J. Han and C. W. Zhou, *Applied Physics Letters*, 2003, **82**, 1613-1615.
16. S. Q. Li, Y. X. Liang and T. H. Wang, *Applied Physics Letters*, 2005, **87**, 1613-1615.
17. D. H. Zhang, Z. Q. Liu, C. Li, T. Tang, X. L. Liu, S. Han, B. Lei and C. W. Zhou, *Nano Letters*, 2004, **4**, 1919-1924.
18. S. Kar, S. Chakrabarti and S. Chaudhuri, *Nanotechnology*, 2006, **17**, 3058-3062.
19. A. Timoumi, H. Bouzouita, M. Kanzard and B. Bezig, *Thin Solid Films,* 2005, **480-481**, 124-128.

20. K. H. Park, K. Jang and S. U. Son, *Angew. Chem. Int. Ed.*, 2006, **45**, 4608-4612.
21. P. Zhao, T. Huang and K. Huang, *J. Phys. Chem. C.*, 2007, **111**, 12890-12897.
22. Y. He, D. Li, G. Xiao, W. Chen, Y. Chen, M. Sun, H. Huang, X. Fu, *J. Phys. Chem. C.*, 2009, **113**, 5254-5262.
23. Y. H. Kim, J. H. Lee, D. W. Shih, S. M. Park, J. S. Moon, J. G. Nam, J. B. Yoo, *Chem. Commun.*, 2010, **46**, 2292-2294.
24. H. Li, C. Chen, X. Huang, Y. Leng, M. Hou, X. Xiao, J. Bao, J. You, W. Zhang, Y. Wang, J. Song, Y. Wang, Q. Liu and G. A. Hope, *Journal of Power Sources*, 2014, **247**, 915-919.
25. X. Yang, J. Xu, T. Wong, Q. Yang and C.-S. Lee, *Physical Chemistry Chemical Physics*, 2013, **15**, 12688-12693.
26. Z. Sun, A. Kumbhar, K. Sun, Q. Liu and J. Fang, *Chemical Communications*, 2008, DOI: 10.1039/b719176f, 1920-1922.
27. T. Nomura, Y. Kousaka, M. Alonso and M. Fukunaga, *Journal of Colloid and Interface Science*, 2000, **223**, 179-184.
28. M. Lee and K. Yong, *Nanotechnology*, 2012, **23**, 194014.
29. N. Skold, L. S. Karlsson, M. W. Larsson, M. E. Pistol, W. Seifert, J. Tragardh and L. Samuelson, *Nano Letters*, 2005, **5**, 1943-1947.
30. P. Caroff, M. E. Messing, B. M. Borg, K. A. Dick, K. Deppert and L.-E. Wernersson, *Nanotechnology*, 2009, **20**, 495606.
31. X. Fan, M.-L. Zhang, I. Shafiq, W.-J. Zhang, C.-S. Lee and S.-T. Lee, *Advanced Materials*, 2009, **21**, 2393-2396.
32. Y. Myung, D. M. Jang, T. K. Sung, Y. J. Sohn, G. B. Jung, Y. J. Cho, H. S. Kim and J. Park, *Acs Nano*, 2010, **4**, 3789-3800.
33. E. Ertekin, P. A. Greaney, D. C. Chrzan and T. D. Sands, *Journal of Applied Physics*, 2005, **97**, 114325.
34. C.-H. Ho, C.-H. Chan, L.-C. Tien and Y.-S. Huang, *Journal of Physical Chemistry C*, 2011, **115**, 25088-25096.
35. C.-H. Ho and Y.-P. Wang, *Optical Materials Express*, 2013, **3**, 1420-1427.
36. Y.-F. Lin and Y.-J. Hsu, *Applied Catalysis B-Environmental*, 2013, **130**, 93-98.
37. X. Wang, H. Zhu, Y. Xu, H. Wang, Y. Tao, S. Hark, X. Xiao and Q. Li, *Acs Nano*, 2010, **4**, 3302-3308.
38. B. Pejova and I. Bineva, *Journal of Physical Chemistry C*, 2013, **117**, 7303-7314.
39. F. Ye, G. Du, Z. Jiang, Y. Zhong, X. Wang, Q. Cao and J. Z. Jiang, *Nanoscale*, 2012, **4**, 7354-7357.
40. H. P. Song, A. L. Yang, H. Y. Wei, Y. Guo, B. Zhang, G. L. Zheng, S. Y. Yang,

X. L. Liu, Q. S. Zhu, Z. G. Wang, T. Y. Yang and H. H. Wang, *Applied Physics Letters*, 2009, **94**, 222114.

41. C. J. Dong, W. X. Yu, M. Xu, J. J. Cao, C. Chen, W. W. Yu and Y. D. Wang, *Journal of Applied Physics*, 2011, **110**, 073712.
42. R. D. Schaller, M. Sykora, S. Jeong and V. I. Klimov, *Journal of Physical Chemistry B*, 2006, **110**, 25332-25338.
43. C. H. Wang, T. T. Chen, Y. F. Chen, M. L. Ho, C. W. Lai and P. T. Chou, *Nanotechnology*, 2008, **19**, 115702.
44. K. Hantke, J. D. Heber, C. Schlichenmaier, A. Thranhardt, T. Meier, B. Kunert, K. Volz, W. Stolz, S. W. Koch and W. W. Ruhle, *Physical Review B*, 2005, **71**, 165320.
45. W. Du, J. Zhu, S. Li and X. Qian, *Crystal Growth & Design*, 2008, **8**, 2130-2136.
46. Y. He, D. Li, G. Xiao, W. Chen, Y. Chen, M. Sun, H. Huang and X. Fu, *Journal of Physical Chemistry C*, 2009, **113**, 5254-5262.
47. X. Fu, X. Wang, Z. Chen, Z. Zhang, Z. Li, D. Y. C. Leung, L. Wu and X. Fu, *Applied Catalysis B-Environmental*, 2010, **95**, 393-399.
48. S. Rengaraj, S. Venkataraj, C.-W. Tai, Y. Kim, E. Repo and M. Sillanpaa, *Langmuir*, 2011, **27**, 5534-5541.

Figure Captions

Figure 1. FE-SEM images of (a) as-grown In_2O_3 nanowires; In_2O_3 nanowires after sulfurization by TAA at given pH solutions: (b) pH=6; (c) pH=4; (d) pH=2. Inset shows optical image of sample.

Figure 2. XRD patterns of as-grown In_2O_3 nanowires and In_2O_3 nanowires after sulfurization by TAA precursor at different pH values.

Figure 3. (a) TEM image of α-In_2S_3 hierarchial nanostructures synthesized at pH=2. (b) TEM image of a single In_2S_3 hierarchial nanostructure. (d) selected-area diffraction patterns of single In_2S_3 hierarchial nanostructure taken along [111] and (d) [332] zone axis.

Figure 4. (a) TEM image, (b) EDX line-scan profile, and (c) EDX elemental mapping of a single α-In_2S_3/In_2O_3 nanowire heterostructure synthesized at pH=6. (d) TEM image, (e) EDX line-scan profile, and (f) EDX elemental mapping of a single α-In_2S_3/In_2O_3 nanowire heterostructure synthesized at pH=4.

Figure 5. (a) PL and (b) UV-visible absorption spectra of as-grown In_2O_3 nanowires and α-In_2S_3/In_2O_3 nanowire heterostructures.

Figure 6. (a) Full-survey, (b) In 3*d*, (c) O 1*s*, (d) S 2*p*, and (e) valence band XPS spectra of as-grown In_2O_3 nanowires and α-In_2S_3/In_2O_3 nanowire heterostructures.

Figure 7. Schematic diagram for the band offset in (a) α-In_2S_3 nanoparticle/In_2O_3 nanowire and (b) α-In_2S_3/ In_2O_3 core-shell nanowire.

Figure 8. Time-resolved photoluminescence spectra of In_2O_3 nanowires and α-In_2S_3/In_2O_3 nanowire heterostructures.

Figure 9. (a) Visible-light driven photocatalytic performance of In_2O_3 nanowires and α-In_2S_3/In_2O_3 nanowire heterostructures. (b) Photocatalytic stability test on α-In_2S_3 nanoparticle/In_2O_3 nanowire heterostructure.

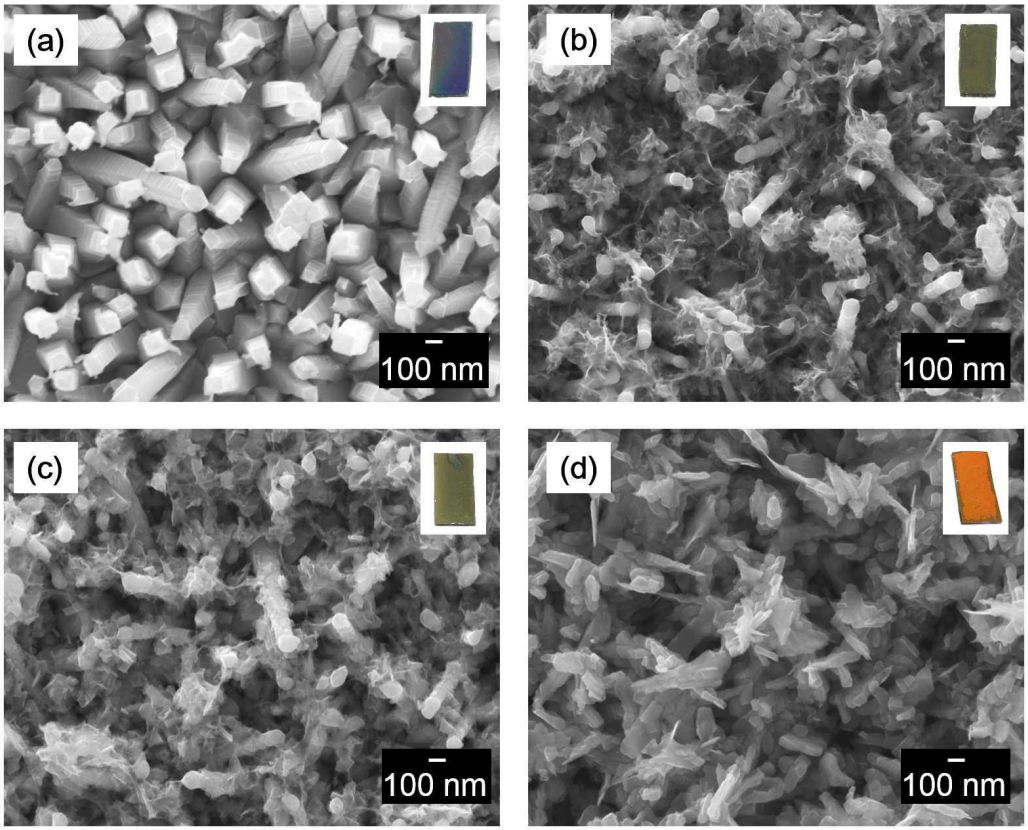

Figure 1. *Tien et al.*

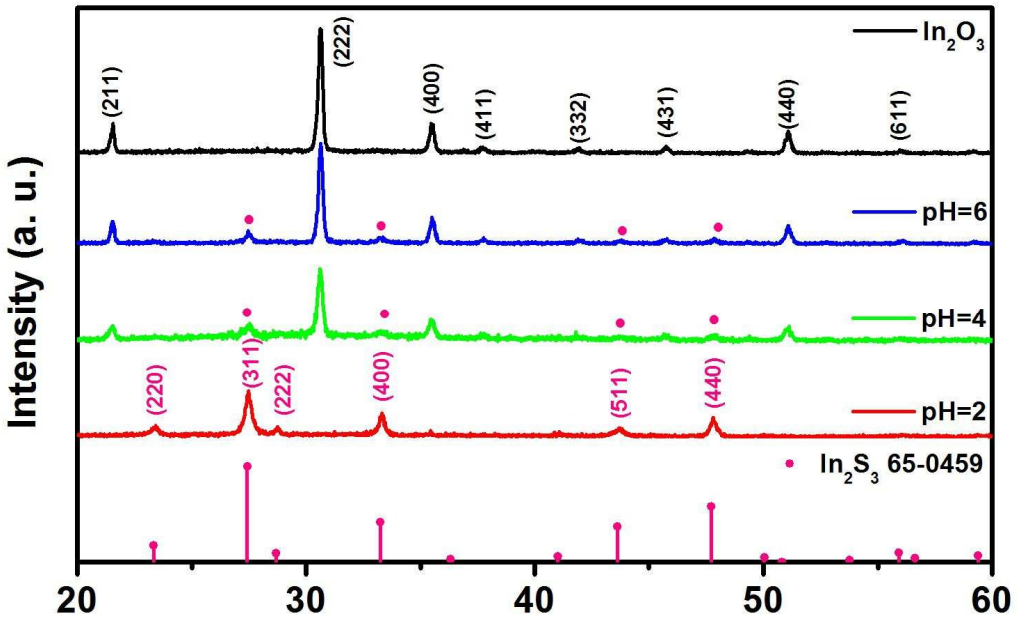

Figure 2. *Tien et al.*

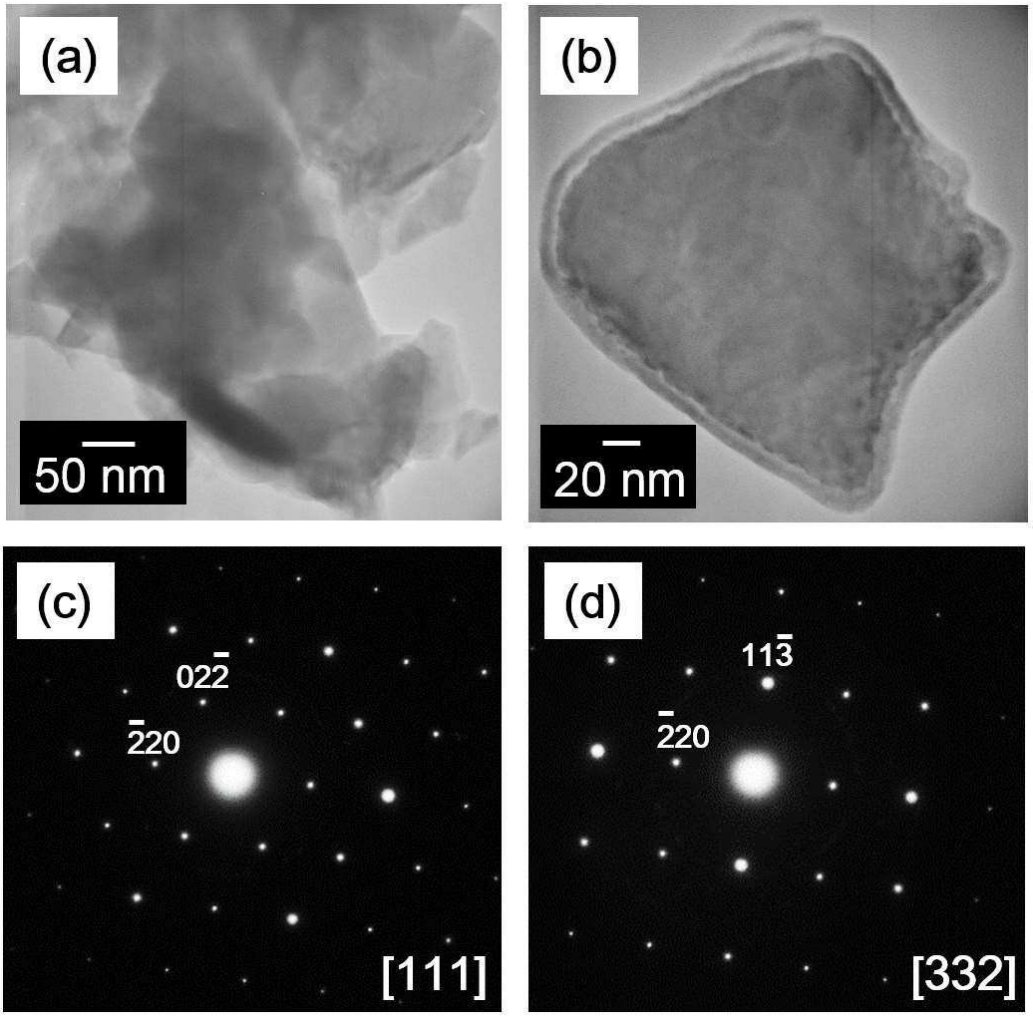

Figure 3. *Tien et al.*

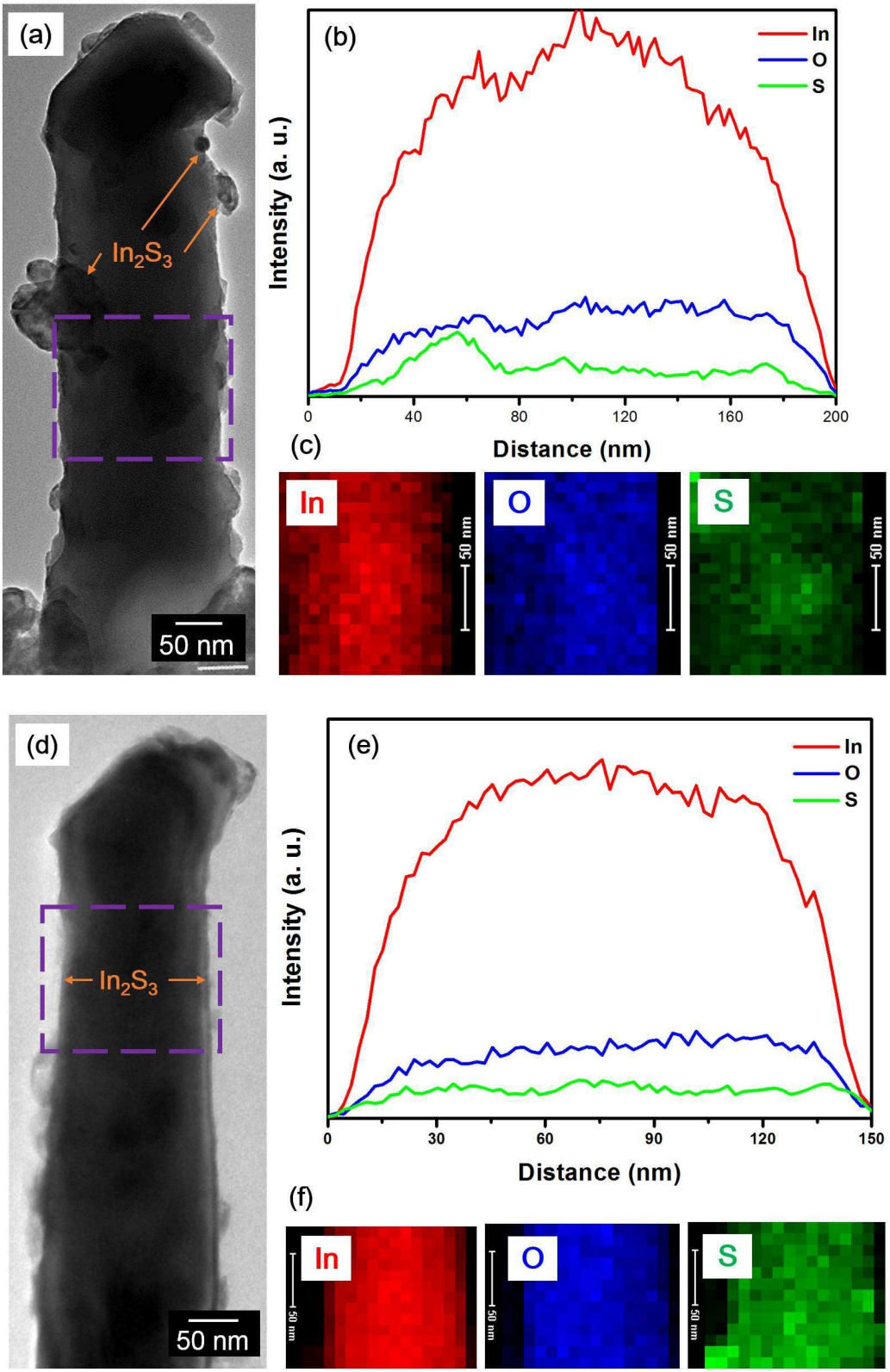

Figure 4. *Tien et al.*

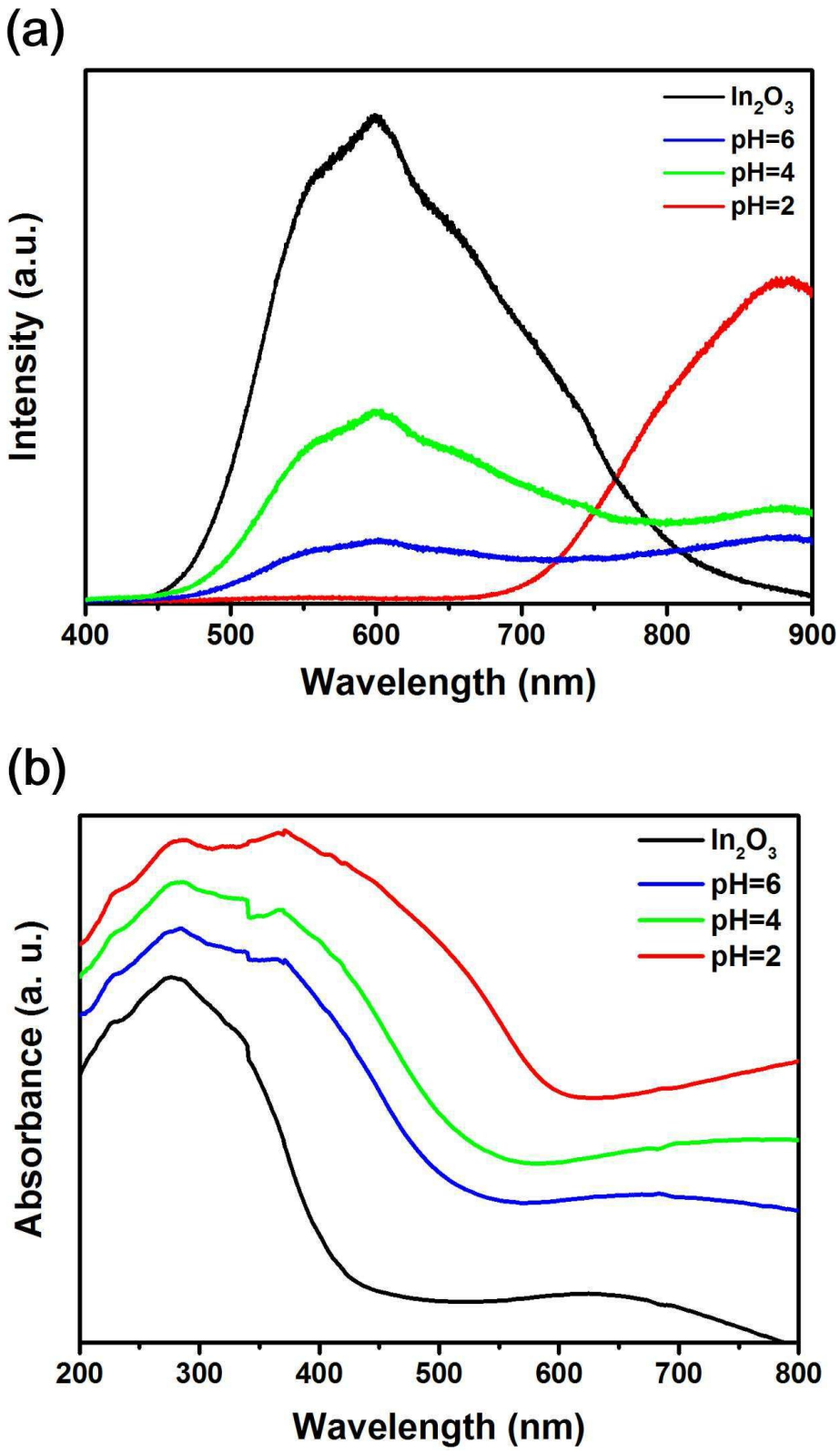

Figure 5. *Tien et al.*

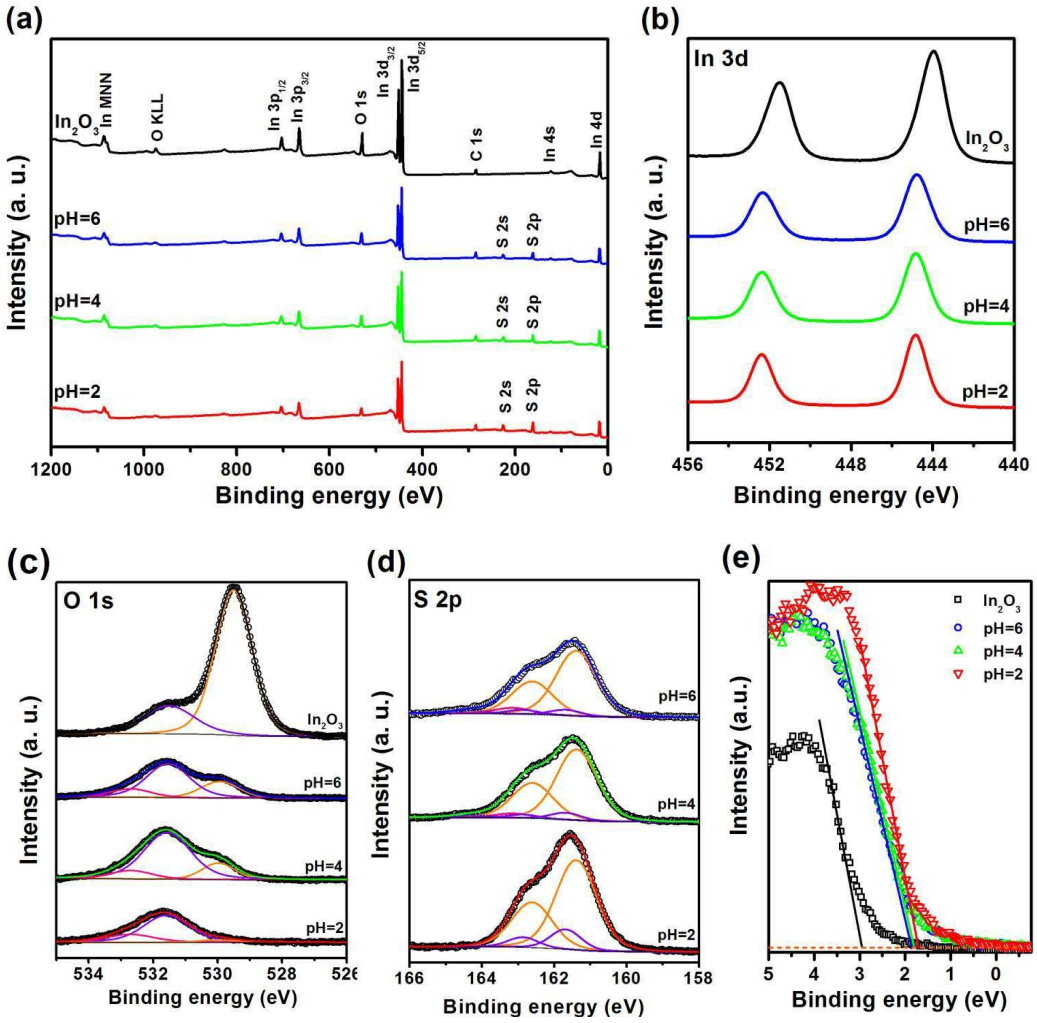

Figure 6. *Tien et al.*

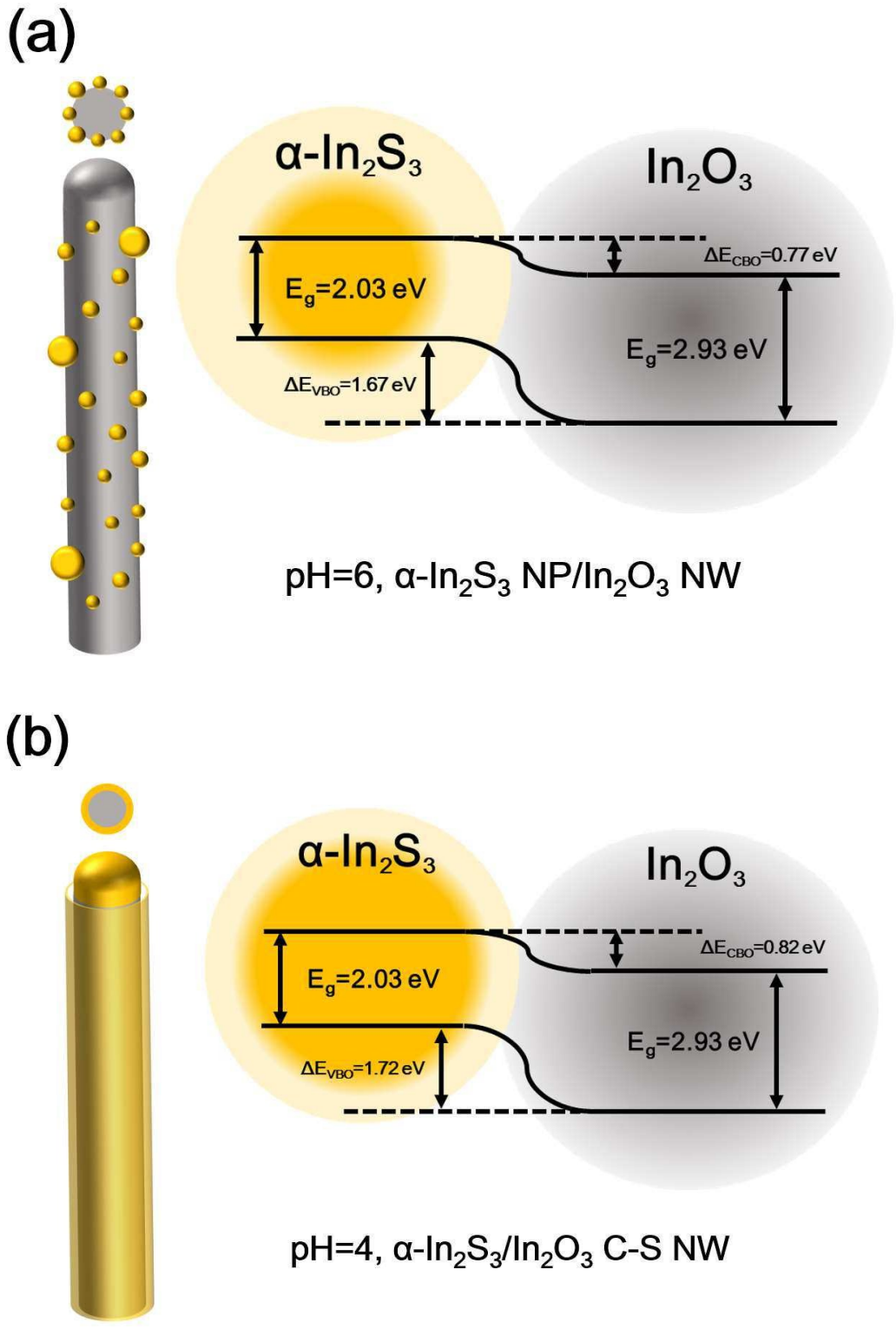

Figure 7. *Tien et al.*

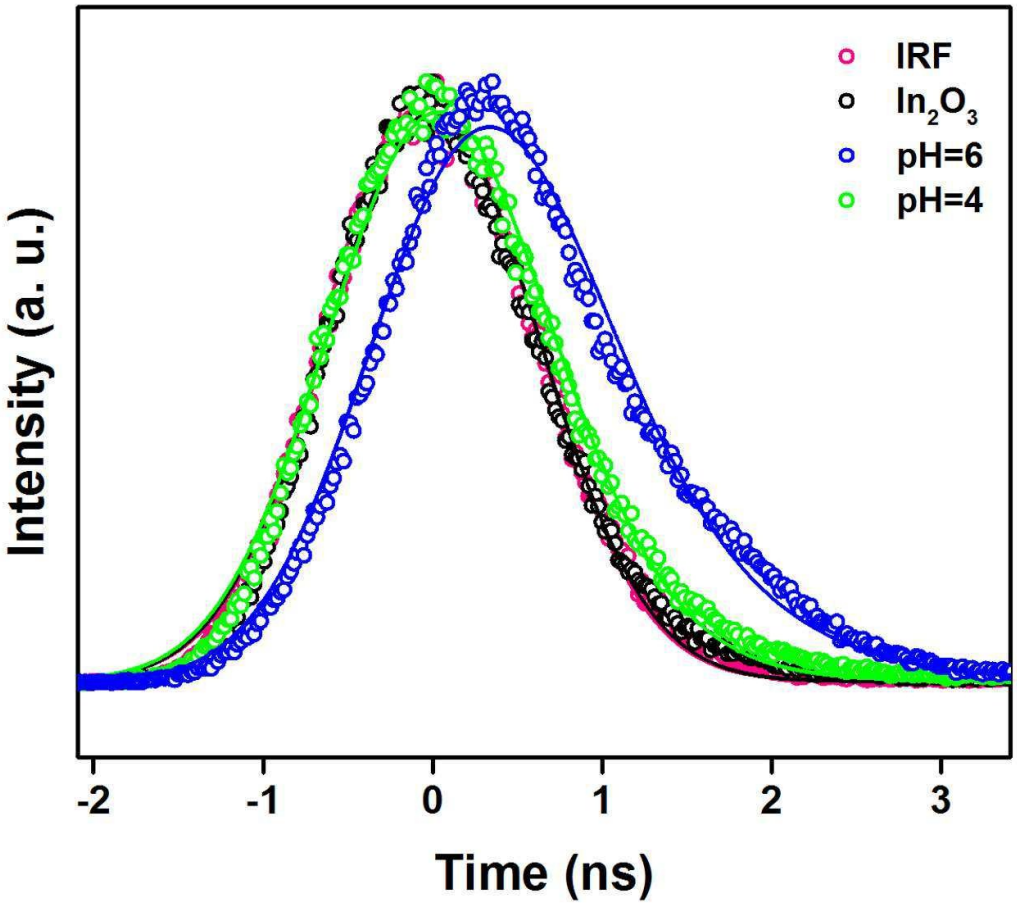

Figure 8. *Tien et al.*

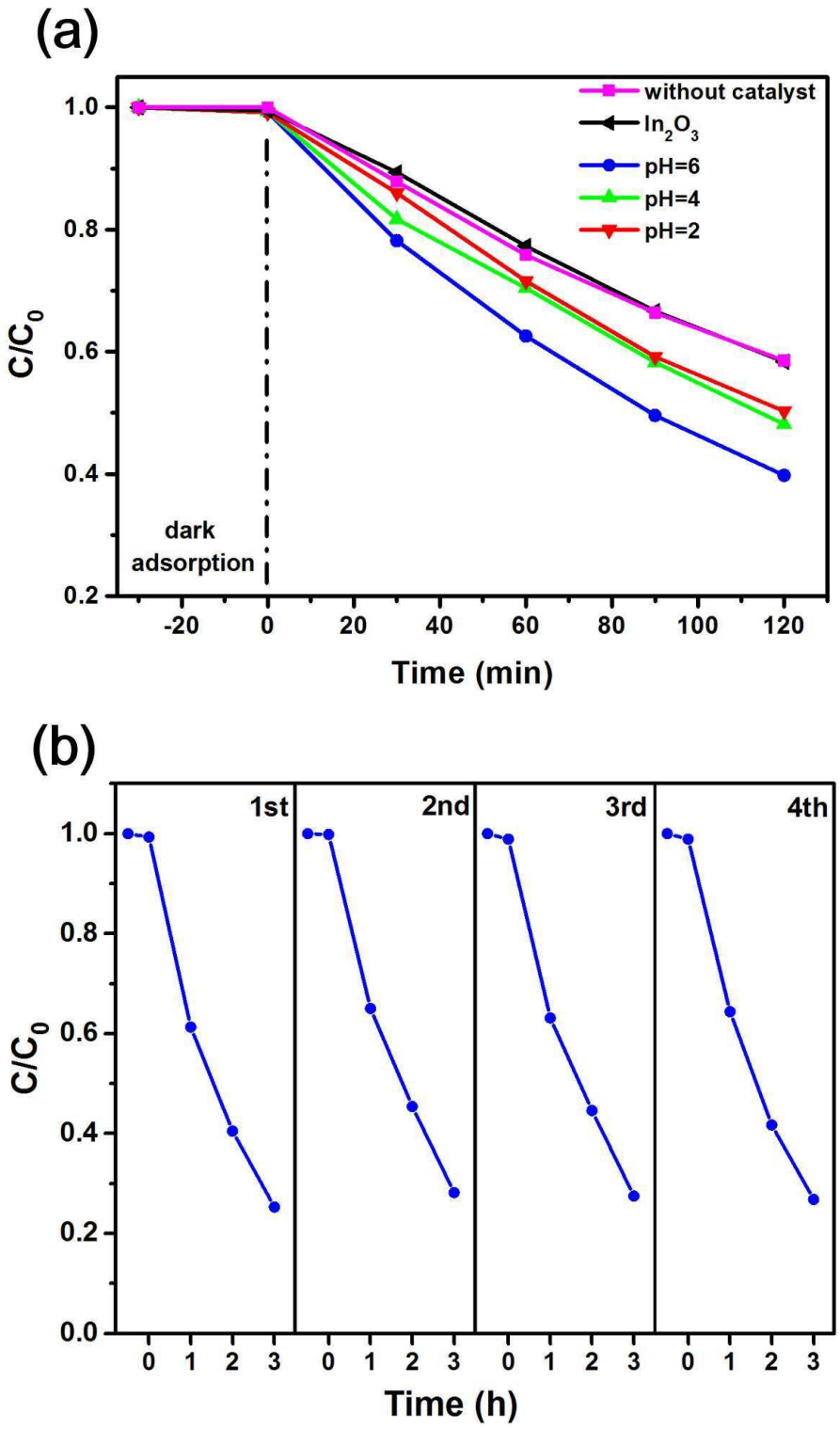

Figure 9. *Tien et al.*

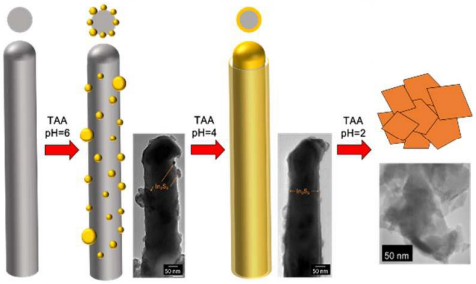

Type-II α-In_2S_3/In_2O_3 nanowire heterostructures exhibit significant photo-induced carrier life time improvement and visible-light-driven photocatalytic activity.